J. Fluid Mech. (2005), *vol.* 532, *pp.* 53–62.
doi:10.1017/S0022112005004180 Printed in the United Kingdom

Forces on a high-Reynolds-number spherical bubble in a turbulent flow

By AXEL MERLE, DOMINIQUE LEGENDRE AND JACQUES MAGNAUDET

Institut de Mécanique des Fluides de Toulouse – UMR CNRS/INPT/UPS 5502, 2, Avenue Camille Soula, 31400 Toulouse, France

(Received 3 January 2005 and in revised form 1 February 2005)

The forces acting on a clean spherical bubble fixed on the axis of a turbulent pipe flow are computed using large-eddy simulation for a bubble Reynolds number $Re_B = 500$ (based on the bubble diameter and centreline velocity in the pipe) and a bulk Reynolds number $Re = 6000$ (based on the pipe diameter and bulk velocity). The force is found to be influenced by all the length and time scales down to the Kolmogorov microscales. The results show that the lift force experiences much larger fluctuations than the drag force, an effect which is shown to be specific to clean bubbles as compared with solid spheres. Using the instantaneous undisturbed velocity and vorticity at the centre of the bubble, the drag force is well predicted by Moore's drag law while Auton's expression for the shear-induced lift force yields a good description of the transverse force.

1. Introduction

The mechanisms that control the motion of spherical particles moving in simple laminar unbounded flows are currently fairly well understood; in particular, the various forces acting on them (drag, history, added mass and shear-induced lift) have been characterized and expressed in a wide range of flow regimes thanks to a combination of analytical studies, experiments and numerical simulations. For a clean spherical bubble moving at high Reynolds number ($Re_B = \rho d \|\boldsymbol{V}_0 - \boldsymbol{V}_B\|/\mu > 50$), the force balance on the bubble is usually written in the form (Auton, Hunt & Prud'homme 1988; Magnaudet & Eames 2000):

$$C_M \frac{\pi d^3}{6}\rho \frac{\mathrm{d}\boldsymbol{V}_B}{\mathrm{d}t} = C_D \frac{\pi d^2}{8}\rho \,\|\boldsymbol{V}_0 - \boldsymbol{V}_B\|\,(\boldsymbol{V}_0 - \boldsymbol{V}_B) - \frac{\pi d^3}{6}\rho \boldsymbol{g} + (1 + C_M)\frac{\pi d^3}{6}\rho \left(\frac{\partial \boldsymbol{V}}{\partial t} + \boldsymbol{V}\cdot\nabla\boldsymbol{V}\right)_0 + C_L \frac{\pi d^3}{6}\rho\,(\boldsymbol{V}_0 - \boldsymbol{V}_B) \times \boldsymbol{\Omega}_0 \quad (1.1)$$

where d and $\boldsymbol{V}_B$ are the bubble diameter and velocity, $\boldsymbol{V}$ and $\boldsymbol{\Omega}$ are the instantaneous undisturbed liquid velocity and vorticity (the index $_0$ denotes quantities evaluated at the centre of the bubble), $\boldsymbol{g}$ is the body force, ρ is the liquid density, μ is the liquid viscosity, C_M is the added-mass coefficient ($C_M = 1/2$ for a spherical body), C_D is the drag coefficient and C_L is the shear-induced lift coefficient. In (1.1) the bubble inertia is neglected compared to the liquid inertia and the so-called history force is neglected compared to the quasi-steady drag (this hypothesis is correct as long as the relative acceleration is not large compared to $\|\boldsymbol{V}_0 - \boldsymbol{V}_B\|^2/d$). For moderate shear rates (typically $\|\boldsymbol{\Omega}_0\|d/\|\boldsymbol{V}_0 - \boldsymbol{V}_B\| < 0.4$), the lift coefficient is close to Auton's theoretical prediction $C_L = 1/2$ (Legendre & Magnaudet (1998) found $C_L = 0.5 - 6.5/Re_B$ for

Re_B	Re	$Re^\star$	D/d	η/d	λ/d	Λ/d	I
500	6000	400	15.6	0.12	1.35	3.1	0.064

TABLE 1. Reynolds numbers and characteristic length scales. Re_B and Re are defined in the text, $Re^\star = Du^\star/\nu$ is the friction Reynolds number based on the friction velocity $u^\star$, η is the Kolomogorov scale, λ is the Taylor microscale, Λ is the integral scale and $I = \langle u'^2 + v'^2 + w'^2\rangle^{1/2}/\sqrt{3}\langle U_a\rangle$ is the relative turbulence intensity (all evaluated on the centreline).

$Re_B > 5$) and the drag coefficient follows Moore's prediction $C_D = (48/Re_B)(1 - 2.211Re_B^{-1/2})$ (Moore 1963) when $Re_B > 50$. Note that in the low-Reynolds-number regime, the drag evolution is significantly modified from this, and the structure of the lift force differs from that in (1.1) since both strain and vorticity combine in a nonlinear way to produce $O(Re_B^{1/2})$ lift forces. The above results are *a priori* valid only when the particle size and the time scale $d/\|\boldsymbol{V}_0 - \boldsymbol{V}_B\|$ are much smaller than the length and time scales characterizing the variations of the surrounding flow. In such situations, the velocity profile of the base flow can be considered linear over distances of $O(d)$ and the force balance (1.1) can be used safely. However in many practical situations the flow is turbulent and bubbles interact with vortical structures whose size is comparable with or smaller than d and whose time scale is much smaller than $d/\|\boldsymbol{V}_0 - \boldsymbol{V}_B\|$. The aim of this study is to evaluate the forces acting on a bubble whose size is comparable with or larger than some eddy scales of the turbulent field. For this purpose, we use the large-eddy simulation (LES) technique to analyse the interaction between a clean spherical bubble and a turbulent pipe flow. The basic question we consider is that of the modification of the force balance (1.1). An equivalent study was recently performed using direct numerical simulation (DNS) by Bagchi & Balachandar (2003) for a solid sphere embedded in a frozen isotropic turbulence.

2. Statement of the problem

We consider a spherical bubble of diameter d set fixed at $x = 0$ on the axis $\boldsymbol{e}_x$ of a circular pipe of diameter D and length L. The Cartesian coordinate system attached to the bubble is (x, y, z). The problem depends on two characteristic numbers: the bubble Reynolds number $Re_B = \rho\langle U_a\rangle d/\mu$, $\langle U_a\rangle$ being the time-averaged centreline velocity of the flow, and the bulk Reynolds number Re. In what follows we shall focus on results obtained for $Re_B = 500$ and $Re = 6000$, selected so that the size of the bubble is comparable with the Taylor microscale of the flow and is about ten times the Kolmogorov microscale. The ratios between these turbulent scales and the bubble diameter are listed in table 1. Note that, given the ratio d/D, the mean flow seen by the bubble is almost uniform with a velocity $\langle U_a\rangle$ and Re_B may be interpreted as the average Reynolds number of the bubble. Note also that in most low-viscosity fluids, a bubble corresponding to $Re_B = 500$ would be strongly deformed, as bubbles rising in still water for instance can only be considered spherical for $Re_B < 250$, approximately. However, as mentioned in the introduction, the dynamics of a clean spherical bubble are qualitatively almost independent of the Reynolds number for $Re_B > 50$, so that the conclusions of the present study are of direct use for gas bubbles rising in water in the range $50 < Re_B < 250$.

The instantaneous force acting on the bubble will be compared with the force $\boldsymbol{F}_{Lam}$ that would be experienced by the same bubble embedded in a laminar, uniform steady

flow having velocity $\langle U_a \rangle$. According to the force balance (1.1),

$$\boldsymbol{F}_{Lam} = 6\pi\mu d\left(1 - 2.211 Re_B^{-1/2}\right)\langle U_a \rangle \boldsymbol{e}_x \tag{2.1}$$

We assume the bubble to be clean (i.e. free of any surfactant or contaminant) and the surface tension to be high enough for its shape to remain spherical. Under these conditions, the normal velocity and tangential stress are zero at the bubble surface. In addition we enforce a non-slip condition at the pipe wall while a periodic condition is imposed at the inlet and outlet of the pipe. The flow in the pipe is driven by imposing a pressure difference ΔP between the outlet and the inlet. The averaged momentum balance in the pipe implies that ΔP is directly related to the average shear stress $\rho u^{\star 2}$ at the pipe wall and to the average force $\langle F \rangle$ acting on the bubble through $\Delta P/L = -4\rho u^{\star 2}/D - 4\langle F \rangle/\pi D^2 L$. Since L and D are both large compared to d, the contribution of $\langle F \rangle$ is negligibly small compared to that of the average wall shear stress.

3. Numerical procedure

The computations reported below were carried out with the LES curvilinear version of the JADIM code described in previous references from our group. Details concerning the discretization of the three-dimensional unsteady Navier–Stokes equations in a general system of orthogonal curvilinear coordinates may be found in Magnaudet, Rivero & Fabre (1995) and Legendre & Magnaudet (1998). The LES procedure which makes use of the dynamic mixed model proposed by Zang, Street & Koseff (1993) was extensively described in Calmet & Magnaudet (1997). The discretization of the governing equations is performed on a staggered mesh and the equations are integrated in space using a finite-volume method with second-order accuracy, all spatial derivatives being approximated using second-order centred schemes. Time advancement is achieved through a Runge–Kutta/Crank–Nicolson algorithm which is second-order accurate in time, incompressibility being satisfied at the end of each time step through a projection technique. The computations employ the grid system described in Legendre & Magnaudet (1998). A plane grid is first generated by considering the streamlines and the equipotentials of the unbounded flow around a circular cylinder. This grid is then made three-dimensional by a rotation about the x-axis. At large distance from the bubble, one of the families of the coordinate lines tends to be parallel to the $\boldsymbol{e}_x$-axis while the other tends to be orthogonal to $\boldsymbol{e}_x$, ensuring a direct matching with the pipe wall, inlet and outlet of the numerical domain.

The length of the computational domain is chosen in order that (i) two-points correlations are negligibly small for separation distances of the order of half the pipe length, (ii) the velocity defect in the bubble wake has significantly decreased so that the re-entering wake due to the periodic condition does not induce any significant change on the upstream flow seen by the bubble. Taking into account the foregoing considerations, we select $L = 5D = 78d$. Figure 1(a) shows that the above two requirements are well satisfied with this choice of L. The grid spacing must satisfy requirements coming from both the LES of the flow and the description of the boundary layer and wake of the bubble. Following Calmet & Magnaudet (1997) the grid is distributed so that 5 points lie within the viscous sublayer near the pipe wall. Consequently we choose a grid spacing $\Delta y^+ = 0.5$ at the wall, corresponding to $\Delta y/D = 0.0014$. We also require that all scales are resolved in the vicinity of the bubble, which according to Legendre & Magnaudet (1998) is achieved if at least three cells lie within the bubble boundary layer. An estimate of the thickness of this boundary layer

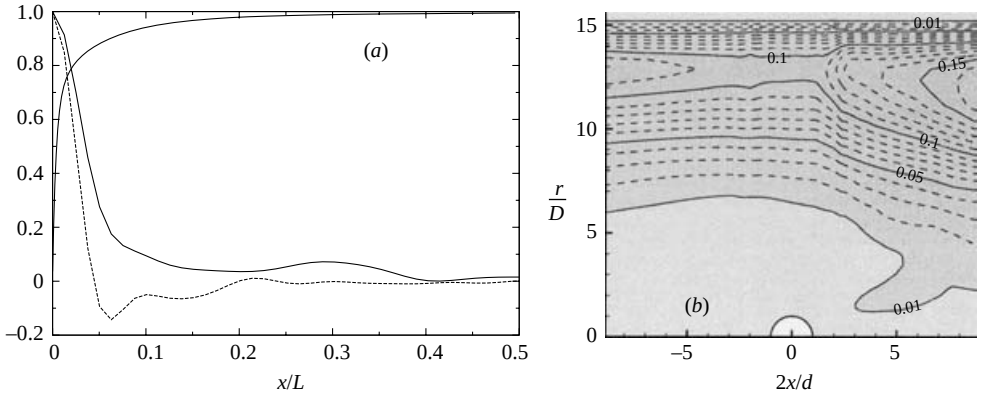

FIGURE 1. (*a*) Two-point correlations: ——, $R_{u'u'}$ and — — —, $R_{v'_r v'_r}$ on the pipe axis versus x/L. ▬▬, Mean centreline velocity downstream of the bubble normalized by $\langle U_a \rangle$ versus x/L (the origin is at the bubble centre). (*b*) Iso-contours of ν_T/ν. The first grey region around the bubble corresponds to $\nu_T < 0.01\nu$.

is $\delta/d \sim Re_B^{-1/2}$ (Moore 1963). The first pressure node is thus located at $0.004\,d$ from the bubble surface. Following Legendre & Magnaudet (1998), the bubble surface is discretized with 20×64 uniformly distributed cells. We also checked that the resulting grid distribution in the vicinity of the bubble allows us to capture the smallest turbulent scales expected in this region. Figure 1(*b*) shows the time-averaged field of the dynamically computed subgrid-scale viscosity ν_T normalized by the fluid kinematic viscosity ν. Clearly, in a large region surrounding the bubble, ν_T/ν is negligibly small. Consequently, the force acting on the bubble can be directly calculated using the resolved pressure and velocity gradients at the bubble surface. Note that ν_T is also negligibly small near the pipe wall thanks to the dynamic procedure. The maximum values of the subgrid-scale viscosity ν_T are found for $5 < r/d < 7$ ($0.3 < r/D < 0.45$) corresponding to the part of the domain where the LES procedure is active. Finally the grid used in the computations reported below is made of $200 \times 52 \times 64$ cells. A constant spacing is used in the azimuthal direction; in the other two directions we select a geometrical distribution of the nodes ensuring that the length ratio between two successive cells is less than 1.15 and 1.2 in the streamwise and radial directions, respectively. The CFL condition yields a time step about 6×10^{-4} times the Kolmogorov time scale, suggesting that all temporal scales of the flow are adequately resolved. We checked the quality of the LES in curvilinear coordinates by considering the turbulent pipe flow at $Re = 6000$ without the bubble. The computations were performed with $80 \times 32 \times 64$ grid points ($\sim 164\,000$ nodes) uniformly spaced in the streamwise and azimuthal directions, the radial distribution being that mentioned above. The results were compared with experiments and numerical simulations reported by Eggels *et al.* (1994). The results of our LES were found to be in good agreement with both the DNS and the experiments for all first- and second-order statistics. An example of this is shown in figure 2. Note that the number of grid points used here is twenty times smaller than that of the reference DNS.

4. Hydrodynamic forces

We now consider the spherical bubble fixed on the axis of the turbulent pipe flow described before. Figure 3 shows a record of the three Cartesian components of the

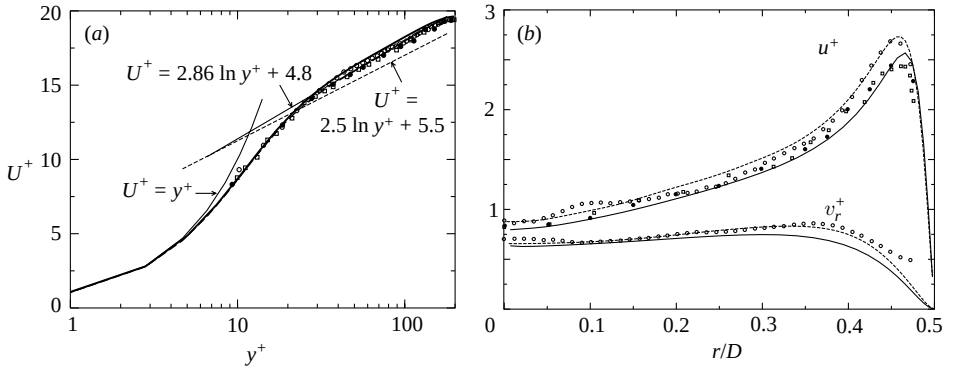

FIGURE 2. (*a*) Mean velocity profiles $U^+(y^+)$ in the wall region. □, ●, ○, experimental data; — — —, DNS; ▬, this study. (*b*) Resolvable turbulent intensities across the pipe: u^+ (streamwise) and v_r^+ (radial) components. □, ●, ○, experiments; — — —, DNS; ——, this study. DNS and experimental data are from Eggels *et al.* (1994).

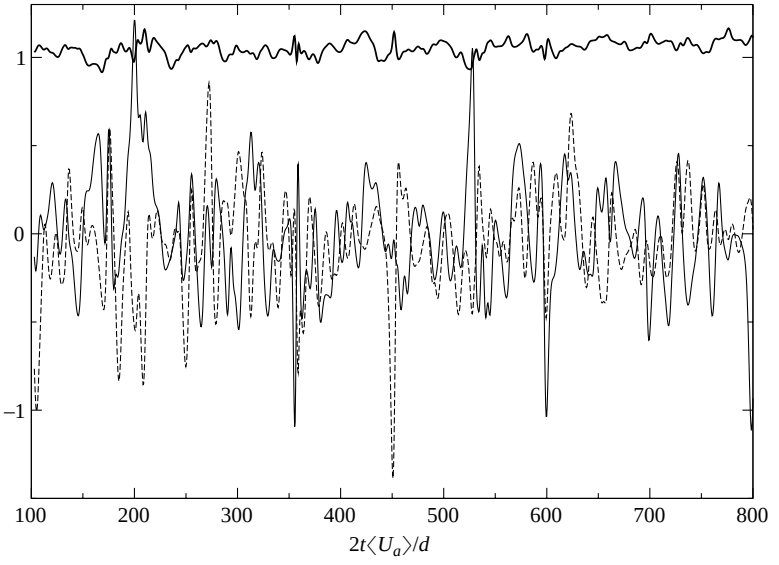

FIGURE 3. Cartesian components of the instantaneous force experienced by the bubble (time is normalized by $d/2\langle U_{axe}\rangle$). ▬, F_x/F_{Lam}; ——, F_y/F_{Lam}; ·····, F_z/F_{Lam}.

F_x/F_{Lam}	F_y/F_{Lam}	F_z/F_{Lam}	$\langle f_x'^2\rangle^{1/2}/F_{Lam}$	$\langle f_y'^2\rangle^{1/2}/F_{Lam} \sim \langle f_z'^2\rangle^{1/2}/F_{Lam}$
~ 1.005	~ 0.008	~ 0.007	0.043	0.27

TABLE 2. Mean values and r.m.s. fluctuations of the components of the force.

instantaneous force experienced by the bubble. The force is normalized by F_{Lam}, the magnitude of the force given by (2.1), whereas time is normalized by the time scale $d/2\langle U_a\rangle$. The mean values of the force and the r.m.s. intensities of the turbulent fluctuations are reported in table 2. Obviously, the dominant force is that acting in the axial direction; its value is found to be close to the drag that the bubble would

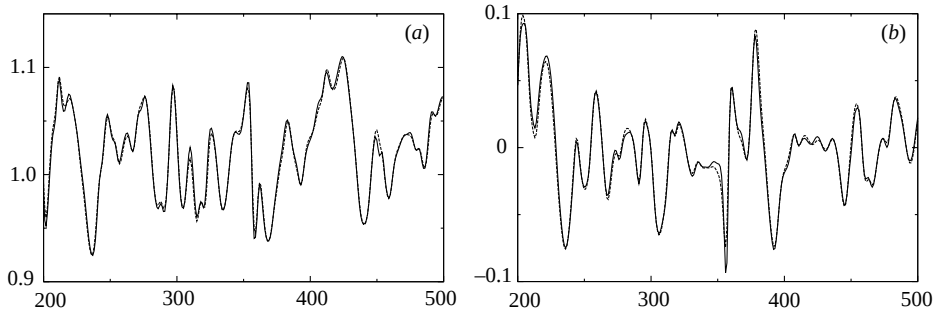

FIGURE 4. Validation of Taylor's hypothesis. ——, $\boldsymbol{V}_0/\langle U_a\rangle$ and – – –, $\boldsymbol{V}_\ell/\langle U_a\rangle$ plotted versus $2t\langle U_a\rangle/d$. (*a*) x-component, (*b*) y-component.

experience in the uniform steady flow corresponding to the mean centreline velocity $\langle U_a\rangle$. Figure 3 clearly shows that the fluctuations observed in the axial direction are much smaller than those in the y- and z-directions, although the time-averaged value of the force is zero in these directions (the average values of F_y and F_z reported in table 2 are not strictly zero due to the finite time over which the average is performed). Moreover, the crosswise fluctuations can instantaneously reach values of the same order as the axial force (see e.g. $t = 110, 350, 530, 600, 800d/2\langle U_a\rangle$ on figure 3) or can be even larger (see e.g. $t = 200, 450d/2\langle U_a\rangle$). This is confirmed by the values reported in table 2 where the r.m.s. intensity of the force fluctuations in the radial direction is found to be six times larger than the axial r.m.s. intensity and represents about 30 % of the mean axial force. This result strongly differs from that obtained in the DNS of Bagchi & Balachandar (2003) who, in the case of a solid sphere embedded in a frozen isotropic turbulence, observed the magnitude of the fluctuations to be similar in the streamwise and crosswise directions. To clarify the origin of this difference, we also performed some computational runs with a rigid sphere instead of a bubble, the particle Reynolds number and size being kept unchanged. In line with the previous authors we obtained much smaller values of the crosswise r.m.s. fluctuations than those reported in table 2 ($\langle f_y'^2\rangle^{1/2}/F_x \sim \langle f_z'^2\rangle^{1/2}/F_x \sim 0.07$ instead of 0.27). Hence it appears that the difference in the value of the crosswise r.m.s. fluctuations of the force is due to the different boundary condition imposed on the sphere and not to a difference in the background turbulence for instance.

Since the instantaneous fluid velocity on the centreline is generally not parallel to the pipe axis, one might suspect that the radial fluctuations simply result from the instantaneous drag. To analyse this possibility, the force may be split into its component parallel to the instantaneous direction of the flow and its transverse component orthogonal to it. Following the classical expression of the forces (1.1), we consider the instantaneous velocity $\boldsymbol{V}$ in the absence of the bubble and evaluate it at the centre of the bubble. Since the flow is turbulent, we have no exact expression for $\boldsymbol{V}_0$. To overcome this problem, we use the well-known Taylor hypothesis and identify $\boldsymbol{V}_0$ with $\boldsymbol{V}_\ell = \boldsymbol{V}(x = -\ell,\ t - \ell/\langle U_a\rangle)$. We chose $\ell \sim 2.5\,d$, a distance at which the bubble-induced disturbance is small since this disturbance is almost irrotational ahead of the bubble. We checked the Taylor hypothesis in the absence of the bubble where $\boldsymbol{V}_0$ can be directly evaluated and compared to $\boldsymbol{V}_\ell$. The axial and y-components of $\boldsymbol{V}_0$ and $\boldsymbol{V}_\ell$ are compared in figure 4 (the z-component yields similar results). The very good collapse of $\boldsymbol{V}_0$ and $\boldsymbol{V}_\ell$ confirms that the Taylor hypothesis can be applied

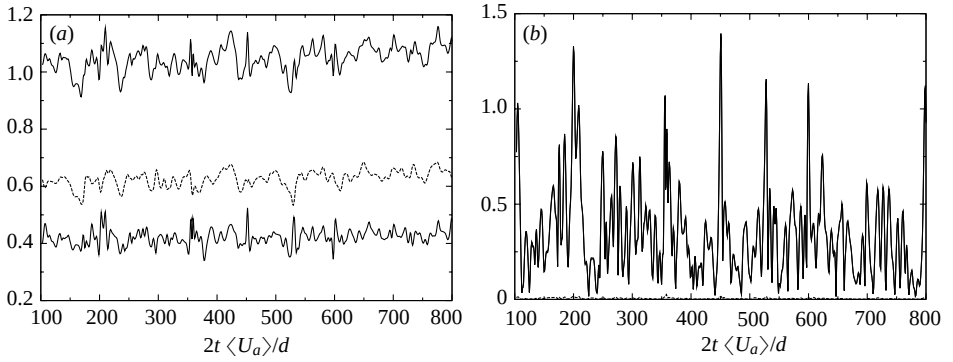

FIGURE 5. —, Pressure and – –, viscous contributions to the force component ▬, normalized with F_{Lam}: (*a*) drag force and (*b*) modulus of the lift force.

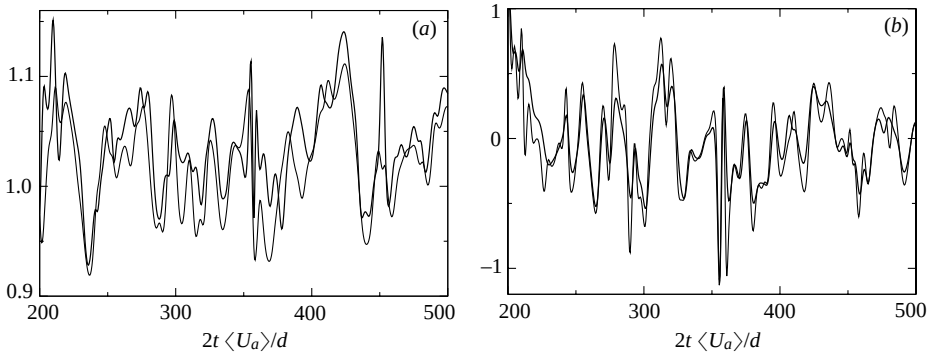

FIGURE 6. Instantaneous drag and lift force. (*a*) Drag: ▬, numerical simulations; —, Moore's drag law (first term of the right-hand side of (1.1)). (*b*) *y*-component of the lift force: ▬, Numerical simulations; —, Auton's prediction (fourth term of the right-hand side of (1.1)).

in the present flow configuration, which is not unlikely since $\langle u_x'^2\rangle^{1/2}/\langle U_a\rangle$ is only about 5 %. A similar agreement was observed for vorticity and velocity gradients.

We can now split the instantaneous force into a contribution along the instantaneous flow direction (hereinafter called the drag contribution) and one orthogonal to $\boldsymbol{V}_0$ (hereinafter called the lift contribution). The corresponding pressure and viscous stress contributions are reported in figures 5(*a*) and 5(*b*) for the drag and lift components, respectively. Both pressure and viscous stress contribute to the drag fluctuations (the latter being about 1.5 times larger than the former as found for high-*Re* bubbles in a laminar flow, see Magnaudet *et al.* 1995) while the lift is only due to the pressure contribution. This behaviour suggests a different origin for the drag and lift components, as in the case of a bubble in a laminar shear flow (see Legendre & Magnaudet 1998). We suspect that the drag fluctuations originate in the viscous dissipation induced by the turbulence fluctuations while the lift is controlled by an inertial mechanism.

The drag and lift components are plotted again in figure 6 and are compared with the instantaneous forces involved in (1.1) (with $\boldsymbol{V}_B = 0$). The drag contribution (figure 6*a*) is fairly well predicted by Moore's expression $\boldsymbol{F}_D = 6\pi\mu d(1 - 2.211/Re_B(t)^{1/2})\boldsymbol{V}_0$ where $Re_B(t) = \rho\|\boldsymbol{V}_0\|d/\mu$ is the instantaneous bubble Reynolds number.

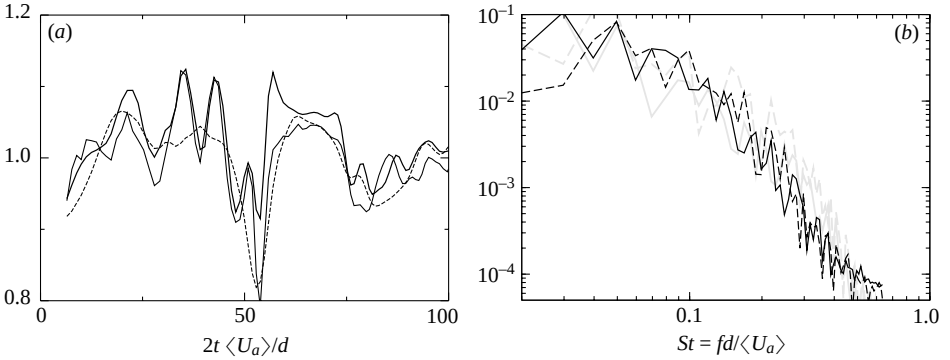

FIGURE 7. (*a*) Instantaneous x-component of the drag force: ——, Numerical simulations; – – –, Moore's drag law (first term of the rhs of 1.1), — Moore's drag law plus added-mass force (first and third terms of the right-hand side of 1.1). (*b*) Spectra of the Cartesian velocity (black lines) and force components (grey lines) normalized by their r.m.s. values: ——, x; – –, y.

The lift or transverse force is also well predicted using Auton's expression $\boldsymbol{F}_L = C_L\rho\frac{1}{6}\pi d^3\boldsymbol{V}_0\times\boldsymbol{\Omega}_0$ with $C_L = 1/2$. In particular, this expression is found to predict the sudden increase of the lift force at time $t = 200d/2\langle U_a\rangle$ displayed in figure 6(*b*). The inertia force induced by the fluid (third term on the right-hand side of (1.1)) also generates contributions to both the drag and the lift component. However, the corresponding effect is small compared to Moore's and Auton's forces because the magnitude of the inertia force may be estimated as $F_i \sim (1 + C_M)\rho\frac{1}{6}\pi d^3[\partial u_i'/\partial t + \langle U_a\rangle\partial u_i'/\partial x + O(u_j'\partial u_i'/\partial x_j)]$. Using again Taylor hypothesis, one has $\partial u_i'/\partial t \sim -\langle U_a\rangle\partial u_i'/\partial x$ from which $F_i \sim O(\partial u_j' u_i'/\partial x_j)$ follows.

Neglecting this contribution we conclude that the dominant force on a high-Reynolds-number spherical bubble fixed in a weakly turbulent flow ($I \ll 1$, see table 1) where turbulence is locally close to homogeneity and isotropy can be approximated as

$$\boldsymbol{F}(t) \sim 6\pi\mu d\left(1 - \frac{2.211}{Re_B(t)^{1/2}}\right)\boldsymbol{V}_0 + C_L\rho\frac{\pi d^3}{6}\boldsymbol{V}_0\times\boldsymbol{\Omega}_0. \tag{4.1}$$

On figure 6(*a*), the main differences between the numerical values of the force and the prediction (4.1) occur at high frequency. We explored the possibility that the inertia force neglected in (4.1) is responsible for most of this discrepancy by adding the third term on the right-hand side of (1.1) to (4.1). The corresponding prediction is reported on figure 7. We observe that the high frequencies are better reproduced. The prediction of the magnitude of the force is also improved.

The agreement between the simple expression (4.1) and the computational results is quite remarkable, keeping in mind that the Moore and Auton expressions were formally derived in flows where the time and length scales are much larger than $d/\langle U_a\rangle$ and d, respectively, whereas the diameter of the bubble considered here is comparable with the Taylor microscale. Indeed the spectra of the time-dependent forces (figure 7*b*) indicate that all flow frequencies are seen by the bubble and contribute to both the drag and the lift force, which confirms that (4.1) (and hence (1.1)) is valid beyond the assumptions under which it was originally established. The agreement of numerical predictions with (4.1) is mostly due to the fact that $\boldsymbol{V}_0$ is dominated by the streamwise component $\langle U_a\rangle\boldsymbol{e}_x$, i.e. advection is dominated by the mean relative velocity, which implies that at leading order the force fluctuations in all three directions depend

linearly on the velocity or vorticity fluctuations. This suggests that Tchen's dispersion theory which is in principle restricted to small particles ($Re_B \ll 1$, $d/\eta \ll 1$) can be extended to larger bubbles with higher Reynolds numbers. Spelt & Biesheuvel (1997) have used this idea for gas bubbles in isotropic turbulence and found it to be consistent with the experimental results of Poorte & Biesheuvel (2002) who studied the motion of $d = 1$ mm gas bubbles in grid turbulence.

The results presented above show that for $Re_B = O(10^2)$, the dynamics of a spherical bubble are correctly predicted by considering the undisturbed liquid velocity and vorticity evaluated at the centre of the bubble. We compared this point-wise description with that based on a local volume average of the flow properties ($\boldsymbol{V}_0$, $\boldsymbol{\Omega}_0$) over volumes of diameter Φ ranging from $d/2$ to $3d$. Such an approach is suggested by the fact that part of the inertia force (that corresponding to the 1 in the $1 + C_M$ term) arises from the volume integral of the fluid acceleration over the bubble volume. Using the averaged flow properties, we computed the drag and lift forces in (4.1) and compared them with the LES results. It turned out that only the mean drag force was accurately predicted whatever Φ, whereas the fluctuations of the force components and their r.m.s. values were severely underpredicted for all $\Phi \neq 0$, the difference between the actual force and the prediction being an increasing function of Φ. For instance, we observed that only about 70 % (resp. 60 %) of the r.m.s. drag (resp. lift) force is captured when $\Phi = d$ is selected, which indicates that about one third of the r.m.s. force fluctuations is due to velocity and/or vorticity fluctuations associated with motions of size smaller than d.

Using previous results, we may also estimate the magnitude of the fluctuations of the forces reported in table 2. First, the instantaneous drag force can be estimated in the form $\boldsymbol{F} \sim 6\pi\mu d[1 - 2.211/Re_B^{1/2} + O(I/Re_B^{1/2})]\boldsymbol{V}_0$ where Re_B is now the time-averaged Reynolds number of the bubble and I is the relative intensity of the turbulence defined in table 1. Coming back to Cartesian coordinates and using the splitting $\boldsymbol{V}_0 = (\langle U_a \rangle + u')\boldsymbol{e}_x + v'\boldsymbol{e}_y + w'\boldsymbol{e}_z$, it follows that the mean value of the force in the axial direction is F_{Lam} whereas the relative r.m.s. value in the same direction is $\langle f_x'^2 \rangle^{1/2}/F_{Lam} \sim \langle u'^2 \rangle^{1/2}/\langle U_a \rangle$. According to figure 2(*b*), $u^+ \sim 1$ on the centreline of the pipe and from table 1 $\langle U_a \rangle/u^\star \sim 20$. The r.m.s. intensity of the axial force can thus be estimated as $\langle f_x'^2 \rangle^{1/2}/F_{Lam} \sim 0.05$ which is in good agreement with the numerical results (see table 2). In the same way the radial r.m.s. intensity resulting from the viscous drag can be estimated as $\langle f_r'^2 \rangle^{1/2}/F_{Lam} \sim \langle v_r'^2 \rangle^{1/2}/\langle U_a \rangle$. Setting $v_r^+ \sim 0.6$ (see figure 2*b*), the radial r.m.s. contribution of the drag is then $\langle f_r'^2 \rangle^{1/2}/F_{Lam} \sim 0.03$ which is one order of magnitude less than the numerical value reported in table 2. This result indicates that the viscous drag contribution to the r.m.s. intensity of the radial force is negligibly small. The radial r.m.s. fluctuations are thus mainly due to the Auton lift force and can be estimated using (4.1). In the y-direction, one finds that the dominant contribution is $\langle f_y'^2 \rangle^{1/2} \sim C_L \rho \pi d^3 \langle U_a \rangle \langle \omega_z'^2 \rangle^{1/2}/6$ where ω_z' is the vorticity fluctuation in the z-direction. As the r.m.s. intensity of the normalized vorticity on the centreline of the pipe is $\langle \omega_z'^2 \rangle^{1/2}/(u^{\star 2}/\nu) \sim 0.038$, we deduce that $\langle f_y'^2 \rangle^{1/2}$ is about 1/3 of the mean drag force in agreement with the result reported in table 2. As a consequence, we conclude that the maximum instantaneous values of the transverse force are induced by the spikes of vorticity whose magnitude is typically 3 times $\langle \omega_z'^2 \rangle^{1/2}$. As pointed out earlier, much smaller values of the crosswise fluctuations of the force are obtained with a rigid sphere (see Bagchi & Balachandar 2003), showing that the lift force on a rigid particle results from a viscous mechanism (even for $Re_B \gg 1$ where it is driven by the asymmetry of the near wake), whereas the lift force on a shear-free spherical bubble is produced by a purely inertial mechanism.

5. Conclusion

The forces experienced by a clean spherical bubble fixed on the axis of a turbulent pipe flow have been computed using LES for bubble Reynolds number $Re_B = 500$ and bulk Reynolds number $Re = 6000$. The results show that these forces are affected by all the time and length scales of the turbulent field down to the Kolmogorov microscales. The values of the instantaneous force reveal that the drag component is fairly well predicted by Moore's drag law while Auton's lift force yields an accurate prediction of the transverse force, even though the diameter of the bubble is comparable with the Taylor microscale. The crosswise r.m.s. fluctuations of the force are much larger than their streamwise counterpart, an effect which is specific to clean bubbles compared with rigid particles, since the mechanism responsible for the lift force differs between these two types of particles. The results obtained here are not specific to a bubble set fixed on the axis of a pipe. They may for instance be applied to isolated bubbles moving in any weakly turbulent flow ($I \ll 1$) in which turbulence is almost homogeneous and isotropic over distances of several bubble diameters. Hence (1.1) can be considered a sound basis for the point-force tracking of high-Re_B ($Re_B > 50$) spherical bubbles, provided the relative turbulence intensity is weak (situations of strong turbulence and weak mean flow where $I = O(1)$ certainly obey different laws). In contrast, note that no conclusion concerning the modelling of the back reaction of the bubbles on the flow can be drawn from our study. Moreover, small bubbles with $Re_B = O(1)$ moving in a turbulent flow will obey different dynamics since the mechanisms responsible for the low-Re lift force differ from those taken into account in (1.1).

REFERENCES

Auton, T. R., Hunt, J. C. R. & Prud'homme, M. 1988 The force exerted on a body in inviscid unsteady non-uniform rotating flow. *J. Fluid Mech.* **197**, 241–257.

Bagchi, P. & Balachandar, S. 2003 Effect of turbulence on the drag and lift of a particle. *Phys. Fluids* **15**, 3496–3513.

Calmet, I. & Magnaudet, J. 1997 Large-eddy simulation of high-schmidt number mass transfer in a turbulent channel flow. *Phys. Fluids* **9**, 438–455.

Eggels, J. G. M., Unger, F., Weiss, M. H., Westerweel, J., Adrian, R. J., Friedrich, R. & Nieuwstadt, F. T. M. 1994 Fully developed turbulent pipe flow: a comparison between direct numerical simulation and experiment. *J. Fluid Mech.* **268**, 175–209.

Legendre, D. & Magnaudet, J. 1998 The lift force on a spherical body in a viscous linear shear flow. *J. Fluid Mech.* **368**, 81–126.

Magnaudet, J. & Eames, I. 2000 The motion of high-reynolds-number bubbles in inhomogeneous flows. *Annu. Rev. Fluid Mech.* **32**, 659–708.

Magnaudet, J., Rivero, M. & Fabre, J. 1995 Accelerated flows past a rigid sphere or a spherical bubble. part 1. steady straining flow. *J. Fluid Mech.* **284**, 97–135.

Moore, D. W. 1963 The boundary layer on a spherical gas bubble. *J. Fluid Mech.* **16**, 161–176.

Poorte, R. E. G. & Biesheuvel, A. 2002 Experiments on the motion of gas bubbles in turbulence generated by an active grid. *J. Fluid Mech.* **461**, 127–154.

Spelt, P. D. M. & Biesheuvel, A. 1997 On the motion of gas bubbles in homogeneous isotropic turbulence. *J. Fluid Mech.* **336**, 221–244.

Zang, Y., Street, R. L. & Koseff, J. R. 1993 A dynamic mixed subgrid-scale model and its application to turbulent recirculating flows. *Phys. Fluids* A **5**, 3186–3196.